# Light-matter coupling and spin-orbit interaction of polariton modes in liquid crystal optical microcavities

E. S. Sedov [1,2,3,4,*] M. M. Glazov,[5,6] P. G. Lagoudakis,[7] and A. V. Kavokin[3,8]

[1]*Key Laboratory for Quantum Materials of Zhejiang Province, Department of Physics, School of Science, Westlake University, 600 Dunyu Road, Hangzhou 310030, Zhejiang Province, China*

[2]*Institute of Natural Sciences, Westlake Institute for Advanced Study, 18 Shilongshan Road, Hangzhou 310024, Zhejiang Province, China*

[3]*Spin Optics Laboratory, St. Petersburg State University, Ulyanovskaya 1, St. Petersburg 198504, Russia*

[4]*Stoletov Vladimir State University, Gorky str. 87, Vladimir 600000, Russia*

[5]*Ioffe Institute, St. Petersburg 194021, Russia*

[6]*Higher School of Economics, National Research University, St. Petersburg 194100, Russia*

[7]*Hybrid Photonics Laboratory, Skolkovo Institute of Science and Technology, Territory of Innovation Center Skolkovo, Bolshoy Boulevard 30, building 1, Moscow 121205, Russia*

[8]*Abrikosov Center for Theoretical Physics, MIPT, Dolgoprudnyi, Moscow Region 141701, Russia*

(Received 9 December 2023; accepted 3 May 2024; published 31 May 2024)

In this theoretical study, we explore the dispersion and basic properties of optical microcavities filled with liquid crystal (LC) media that contain embedded quantum wells. As a result of the strong coupling between cavity photons and excitons, exciton polariton quasiparticles arise in these structures. LC-filled microcavities have an advantage of the ability to manipulate the spin (polarization) of the photonic component of the polariton states by controlling the orientation of LC molecules using an external electric field. This enables the engineering of controllable synthetic Hamiltonians for the polariton eigenmodes in microcavity structures. The introduction of synthetic spin-orbit interaction via placing of the quantum wells at particular positions in the LC-filled cavity enables control over the propagation of exciton polaritons, leading to various spatial effects. Through numerical calculations, we successfully reproduce the birefringence and *zitterbewegung* phenomena exhibited by exciton polaritons propagating within the microcavity plane. We also examine the conditions required for strong coupling when utilizing perovskite layers as hosts for excitons. While the strong coupling regime can be also achieved in this material system, the manifestations of the synthetic spin-orbit interaction are suppressed owing to stronger disorder and nonradiative processes.

DOI: 10.1103/PhysRevResearch.6.023220

## I. INTRODUCTION

Our ability to control a physical system increases with the number of controllable parameters. This general principle applies to optical systems in the same extent as to matter systems. By setting up conditions that allow for the interplay between different control variables, one can control one variable by adjusting another related variable. In the case of light, the spin-orbit interaction (SOI) couples the internal spin variable, which determines light polarization, with its spatial (orbital) variable that governs the spatial distribution of light within an optical structure [1]. The effects of SOI are particularly prominent in composite multi-interface optical structures [2] and are further enhanced when optical components possess optical anisotropy [3–5].

Specially designed optical microcavities combine all the necessary conditions for the occurrence of SOI in light [6]. A microcavity comprises an optically transparent dielectric or semiconductor layer with a thickness on the order of the light wavelength ($\lambda$), sandwiched between two distributed Bragg reflectors (DBRs). The central cavity layer contains narrow sublayers that serve as hosts for matter excitations, excitons, which are in resonance with the cavity modes. These exciton layers can be semiconductor quantum wells (QWs) [7,8], transition metal dichalcogenide monolayers [9,10], or perovskites [11]. When strongly coupled with excitons, the confined cavity photon modes transform into exciton-polariton modes, inheriting properties of both light and matter. These exciton-polaritons exhibit distinct dispersion and fast propagation in the microcavity plane, similar to photons. At the same time, they can be controlled through external manipulation of the exciton component. An alternative approach to achieving strong exciton-photon coupling is through resonant Bragg mirrors, which differ from conventional Bragg mirrors by incorporating QWs within each sublayer of alternating materials [12–14].

The investigation of synthetic SOI for polaritons has gained significant attention in recent years, driven by its

*evgeny_sedov@mail.ru

potential applications in optoelectronics [2,15–18]. The spin of polaritons is closely related to the polarization of their photon component. Optical selection rules dictate that left and right circularly polarized polaritons are formed through the coupling of photons with corresponding polarizations to excitons with angular momentum projections (pseudospins) of $\pm 1$ along the growth axis of QW. In microcavity structures, various mechanisms lead to the splitting of polariton polarization states, resulting in diverse SOI effects.

In conventional solid-state microcavities, the most prominent mechanism of SOI is the splitting of transverse electric (TE) and transverse magnetic (TM) photon cavity modes. This splitting arises from the difference in phase shifts experienced by the modes upon reflection from interfaces. The TE-TM splitting serves as the foundation for several effects, including the optical spin Hall effect [19,20], the *zitterbewegung* [21–23], and the formation of polarization domains in planar polariton waveguides [24], among other phenomena.

Furthermore, a variety of SOI mechanisms in polariton microcavity structures are associated with their exciton component. These mechanisms arise due to the reduced symmetry of QWs or their interfaces. Examples of such mechanisms include exchange-induced anisotropy [25,26], splitting induced by interface roughness and built-in strain [27–29], and splitting induced by external stress [30]. Additionally, Zeeman splitting in an external magnetic field can also occur, both in the Faraday [5,31–34] and Voight [7,22,35] geometries.

Usually, in conventional solid-state microcavities, manipulation of polaritons through SOI is achievable by leveraging their excitonic component, which readily responds to external influences like electric and magnetic fields. A recent area of focus involves a new class of optical microcavities that provide control over pure photonic SOI [36–41]. In these microcavities, the central cavity layer is filled with a nematic liquid crystal (LC). By aligning the LC molecules in a specific direction using an external electric field, it becomes possible to break the equivalence of different propagation directions for linear polarizations within the cavity plane, thus introducing optical anisotropy to the structure.

Previously, in Refs. [36,37], the dispersion properties of LC-filled microcavities without accounting for exciton resonances have been explored. In particular, the synthetic Rashba-Dresselhaus Hamiltonian $\hat{H}_{\rm RD} \propto \hat{\sigma}_z k_y$, has been derived to describe photonic modes, where $\hat{\sigma}_z$ is the third Pauli matrix and $\mathbf{k} = (k_x, k_y)$ is the in-plane wave vector. Several studies [38–40] have investigated strong coupling in LC-filled microcavities using two-dimensional perovskite layers as exciton hosts. These perovskite layers enable extremely strong exciton-photon coupling, resulting in large Rabi splitting reaching hundreds of millielectron volts, making the formation of polaritons feasible at high, up to room temperature [42–44]. However, the presence of perovskites introduces significant nonradiative losses in polaritons, leading to decay rates reaching tens of millielectron volts. Hence, the effects of synthetic SOI are expected to diminish in the perovskite-based LC cavities.

In this paper, we theoretically investigate the SOI of exciton polaritons in LC-filled microcavities, with a specific emphasis on spatial properties. To achieve this, we sacrifice the strength of the exciton-photon coupling by utilizing conventional semiconductor QWs as the matter component of the interaction. However, this approach allows for the manifestation of spatial effects. Importantly, our analysis is conducted within the linear regime where polariton-polariton interactions are negligible. This approach, applicable under conditions of weak incident light intensities, ensures that the results distinctly reflect the SOI effects, unaffected by nonlinear phenomena. In our study, we explore the dispersion properties of LC-filled microcavity structures operating under strong coupling conditions. We construct a synthetic effective light-matter Hamiltonian to characterize the dispersion and general properties of the structure based on its eigenmodes. Additionally, we numerically demonstrate the effects of birefringence and *zitterbewegung* of polaritons, which can be induced in the structure in a controlled manner. We identify the conditions that enable the coupling of two cavity modes, where only one mode exhibits strong coupling with excitons. Furthermore, we analyze the strong coupling in LC-filled microcavities with an embedded two-dimensional perovskite layer demonstrating suppressed SOI effects.

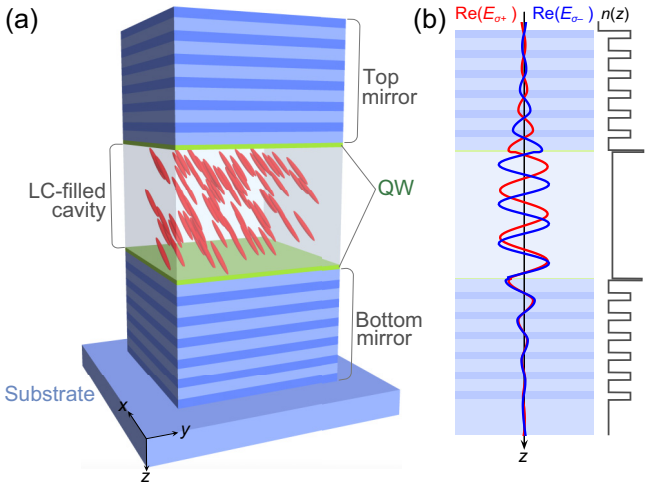


FIG. 1. (a) Schematic of the structure with the LC-filled microcavity layer and two embedded QWs. (b) The electric-field distribution of the orthogonal cavity eigenmodes ($\sigma^+$ and $\sigma^-$) in the structure growth direction $z$ at normal incidence ($k_{x,y} = 0$). The broken line to the right of (b) shows schematic of the real part of the refractive index profile of the structure in the $z$ direction.

## II. DETAILS OF THE STRUCTURE

We consider a structure based on the microcavity discussed in [36], as depicted in Fig. 1(a). This particular structure consists of two DBRs with a layer of LC medium sandwiched between them. In our modification compared to [36], we have included two layers capable of hosting excitons within the central cavity layer. The DBRs are composed of six pairs of $SiO_2/TiO_2$ layers, and their stop bands are centered at 1.515 eV. In each DBR, the layers are arranged such that the $SiO_2$ layer is adjacent to the central cavity layer. The choice of the materials of DBRs takes advantage of the high refractive index contrast $(n_{\rm TiO_2} - n_{\rm SiO_2})/n_{\rm TiO_2} \approx 0.4$, which enables a strong TE-TM splitting effect. The bottom DBR is grown on a $SiO_2$ substrate.

The microcavity layer is filled with a nematic LC medium, which can be regarded as an optically uniaxial medium. The optical axis of the LC medium aligns with the orientation direction of the LC molecules, and this orientation can be controlled by applying an electric field [41]. When the LC molecules are aligned along the $z$ axis, the LC dielectric tensor takes the following form:

$$\hat{\varepsilon}_{\mathrm{LC},0} = \begin{pmatrix} \varepsilon_\perp & 0 & 0 \\ 0 & \varepsilon_\perp & 0 \\ 0 & 0 & \varepsilon_\parallel \end{pmatrix}, \tag{1}$$

where $\varepsilon_\parallel = n_o^2$ and $\varepsilon_\perp$ are the LC dielectric constants. The refractive index of the ordinary wave $n_o$ is immediately determined by the longitudinal component $\varepsilon_\parallel$. In further consideration, we treat LC molecules to be oriented in $xz$ plane. The rotation of the optical axis around $y$ axis by angle $\theta$ leads to the following transformation of the dielectric tensor: $\hat{\varepsilon}_{\mathrm{LC}} = \hat{R}_y(\theta)\hat{\varepsilon}_{\mathrm{LC},0}\hat{R}_y^{-1}(\theta)$ where $\hat{R}_y(\theta)$ is the corresponding rotation matrix. Values of the parameters of the materials that compose the structure used for simulations are given in [45].

As model exciton layers, we use 20-nm-thick GaAs QWs that adjoin the cavity layer. They are characterized by the resonant dielectric function

$$\varepsilon_{\mathrm{QW}} = \varepsilon_{\mathrm{b}}\left(1 + \frac{\omega_{\mathrm{LT}}}{\omega_{\mathrm{exc}} - \omega - i\Gamma}\right), \tag{2}$$

where the exciton resonance energy is $E_{\mathrm{exc}} = \hbar\omega_{\mathrm{exc}} = 1.515\,\mathrm{eV}$, the background dielectric constant is $\varepsilon_{\mathrm{b}} = 3.7^2$, the LT splitting is $\hbar\omega_{\mathrm{LT}} = 0.08\,\mathrm{meV}$, and the nonradiative decay rate is $\hbar\Gamma = 0.1\,\mathrm{meV}$. Alternative designs with a single QW or perovskite layer are described in Secs. V and VI.

## III. ENERGY SPECTRUM AND BASIC PROPERTIES

### A. Calculation approach

To investigate the dispersion properties of the structure, we employ the generalized 4×4 transfer matrix formalism (MF) [46,47], which fully considers light polarization and is capable of handling optical degeneracies that arise in isotropic embedded layers [4,48,49]. The formalism applied to the layered structure of a planar microcavity implies the solution of Maxwell's equations in each of the homogeneous optical layers, accompanied by matching the solutions at the layer interfaces.

In the considered geometry, light is incident from the side of the top DBR towards the substrate. As a plane wave propagates through the structure with a frequency $\omega_0$ and a wave vector $\boldsymbol{k} = (\mathbf{k}, k_z)$, the in-plane components $\mathbf{k} = (k_x, k_y)$ remain unchanged when crossing layer interfaces, while the out-of-plane component $k_z = \omega_0\kappa/c$ adjusts to the dispersion properties of the layers. Here, we introduced the dimensionless propagation constant $\kappa$ for convenience, and $c$ is the speed of light in vacuum. In each layer $j$, the propagation constant $\kappa_j$ is the solution of the Maxwell's equations in this layer, which within the 4×4 MF are reduced to the following eigenvalue problem:

$$\kappa_j\boldsymbol{\Psi}_j = \hat{\Delta}\boldsymbol{\Psi}_j, \tag{3}$$

where $\boldsymbol{\Psi}_j = (E_{x,j}, H_{y,j}, E_{y,j}, H_{x,j})^{\mathrm{T}}$ is the vector of the transverse electric ($E_{l,j}$) and magnetic ($H_{l,j}$) field amplitudes, $l = x, y$, and $\hat{\Delta}$ is the 4×4 characteristic matrix, see details in Appendix and in Refs. [4,47,50].

In the basis of forward (→) and backward (←) propagating waves, the transverse electric field in the layer $j$ can be characterized by the four-component vector

$$\mathbf{E}_j = \begin{pmatrix} E^p_{\rightarrow,j} \\ E^s_{\rightarrow,j} \\ E^p_{\leftarrow,j} \\ E^s_{\leftarrow,j} \end{pmatrix}, \tag{4}$$

where $p$ and $s$ indicate polarization of the vector components. Then two adjacent layers with indices $j-1$ and $j$ are connected with each other as

$$\mathbf{E}_{j-1} = \hat{A}_{j-1}^{-1}\hat{A}_j\hat{P}_j\mathbf{E}_j, \tag{5}$$

where the 4×4 matrix $\hat{A}_j$ is used for projection of the field vector $\mathbf{E}_j$ onto the eigenvector $\boldsymbol{\Psi}_j$ of the layer, while the matrix $\hat{A}_{j-1}^{-1}\hat{A}_j$ is responsible for the fulfillment of the boundary conditions at the interface of the layers. $\hat{P}_j$ is the propagation matrix through the layer $j$. The matrices $\hat{\Delta}$, $\hat{A}_j$ and $\hat{P}_j$ are defined in the Appendix.

The input field $\mathbf{E}_0$ to the structure composed of $N$ layers is linked to the output field $\mathbf{E}_{N+1}$ as

$$\mathbf{E}_0 = \hat{T}\mathbf{E}_{N+1}, \tag{6}$$

where $\hat{A}_0\hat{T}\hat{A}_{N+1}^{-1} = \prod_{j=1}^{N}\hat{A}_j\hat{P}_j\hat{A}_j^{-1}$ is the transfer matrix through the structure. The index $N+1$ characterizes the bulk medium adjacent to the $N$th layer, which is a substrate in our case.

To calculate the propagation in the structure of a light beam of finite-spatial dimensions, one should perform the Fourier transform of the incident beam and apply MF to each $\mathbf{k}$ component.

The matrix $\hat{T}$ allows one to calculate the reflection coefficients for pure $p$- and $s$-polarized incident waves as following: $r_{(pp,ps)} = [T_{(31,41)}T_{22} - T_{(32,42)}T_{21}]/r_0$ and $r_{(ss,sp)} = [T_{(42,32)}T_{11} - T_{(41,31)}T_{12}]/r_0$, where $r_0 = T_{11}T_{22} - T_{12}T_{21}$. The coefficients $r_{pp}$ and $r_{ss}$ characterize reflection without changing its polarization, while $r_{ps}$ and $r_{sp}$ characterize the rotation of the polarization upon reflection due to SOI induced by optical anisotropy of the LC layer.

It should be noted that in the absence of optical anisotropy at $\theta = 0$, the basis (4) indeed consists of $s$ and $p$ polarization waves. The presence of anisotropy, however, leads to a mixing of these polarizations. In this scenario, it is appropriate to describe the propagation through the layers in terms of ordinary and extraordinary waves. Nevertheless, to keep the text concise and avoid introducing new terminology, we continue to use the $s$ and $p$ indices to differentiate the electric field components, regardless of whether the anisotropy is present or not.

### B. Dispersion properties

In order to investigate the dispersion of the eigenmodes in the microcavity, we analyze the minima of its reflectance spectrum $R$, which can be calculated directly from the

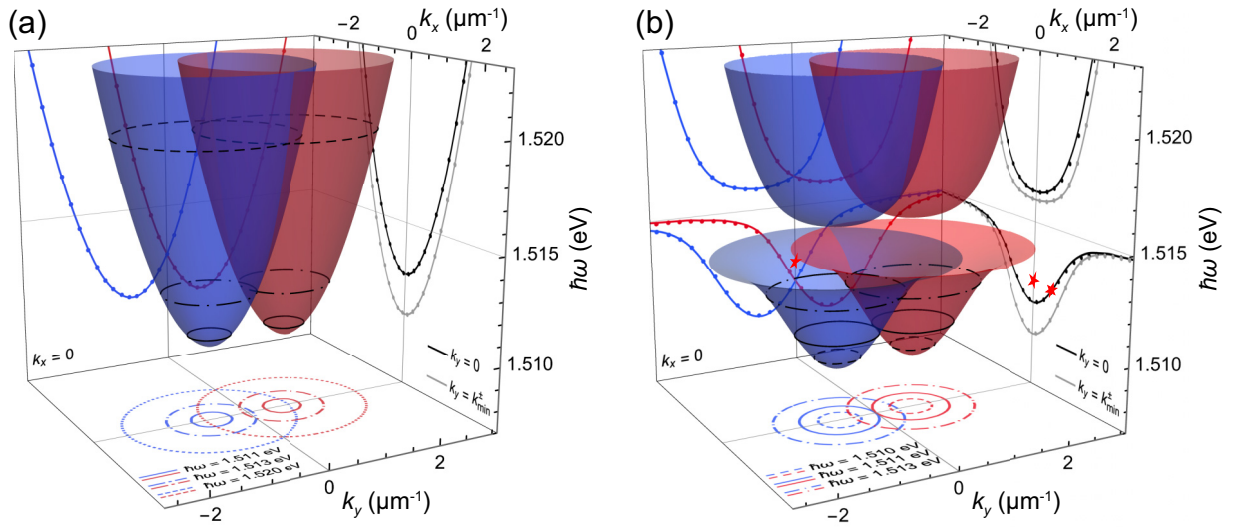


FIG. 2. Dispersion of eigenmodes of the LC-filled microcavity without the exciton resonance (a) and with the exciton resonance at $\hbar\omega_{\rm exc} = 1.515$ eV (b) in embedded QWs obtained by 4×4 MF. The thickness of the cavity layer is $d_c = 1430$ nm, the rotation angle of LC molecules $\theta$ is about 26.52°. The side wall plots and the bottom contours show cross sections of the dispersion surfaces in the specified planes. Solid lines and dots in the side wall plots show dispersions obtained by MF and from the Hamiltonian (19), respectively. Red six-pointed and five-pointed stars in (b) indicate the excitation conditions for Figs. 5(a)–5(e) and 5(f)–5(j), respectively.

amplitude reflection coefficient as $R_{ij} = |r_{ij}|^2$, $i, j = s, p$. Figure 2 shows the reflectivity dispersions obtained for the specific parameters of the structure provided in [45]. In Fig. 2(a), we exclude the exciton resonance while keeping the background dielectric permittivity and the thickness of the QW layers. By adjusting the width $d_c$ of the cavity layer and the LC orientation angle $\theta$, we replicate the photon dispersion observed in an empty LC-filled microcavity studied in [36]. Two split in energy and quasimomentum dispersion branches are inherent in the microcavity that are nonreciprocal with respect to one of the directions, $\omega(k_y) \neq \omega(-k_y)$. The branches exhibit crossing at $k_y = 0$ while their minima are shifted from $\mathbf{k} = 0$ by $(0, k_{\rm min}^{\pm})$.

For the dispersion in Fig. 2(b), the exciton resonance at $\hbar\omega_{\rm exc} = 1.515$ eV is taken into account. The resonance supported by high refractive index contrast in DBRs and by low nonradiative losses in the model QW enabling strong coupling between the cavity modes and QW excitons. As a result, the microcavity exhibits two pairs of dispersion branches of exciton polaritons that retain the nonreciprocity inherited from the photonic fraction. Within each pair, the total splitting is composed of two distinct splittings. The first is the TE-TM splitting of polariton modes, inherent to the layered (multi-interface) structure of the microcavity. This splitting's hallmark is its dependence on the wave vector of the polariton state, vanishing at $k = 0$. Additionally, in scenarios where only this type of splitting is present, the dispersion of the inherent modes remains reciprocal.

The second splitting arises from the anisotropy in the LC-filled microcavity layer, affecting linearly polarized modes within the $XY$ plane. Unlike the TE-TM splitting, this anisotropic splitting introduces a direction where dispersion reciprocity is broken, which in our geometry aligns with the $y$ axis. The magnitude of the splitting can be manipulated through the orientation angle of the LC molecules $\theta$, serving as the control parameter. Adjusting the magnitude of the splitting has a significant impact on the shape and arrangement of the dispersion surfaces.

Figure 3 illustrates how the characteristic points of the dispersion surfaces of the lower in energy scale pair of polariton branches depend on the angle $\theta$. In Fig. 3(a), the red and green curves illustrate the dependence of the polariton energy at the center of the dispersion surfaces $\hbar\omega(0, 0)$ on $\theta$. It is observed that a gap typically exists between the branches. However, at a certain $\theta$ value, this gap closes, leading to a crossing of the dispersion surfaces. This particular angle, approximately 26.52°, was taken for plotting the dispersions depicted in Fig. 2(b).

When the anisotropic splitting is large (LC molecules oriented closer to the $x$ axis), the dispersion surfaces are far apart and do not influence each other. Conversely, when the splitting is small (LC molecules oriented closer to the $z$ axis), its contribution is negligible compared to TE-TM splitting. In both scenarios, away from this critical angle, both dispersion surfaces exhibit a minimum at the point $(k_x, k_y) = (0, 0)$.

As the dispersion surfaces approach each other, and the contributions of the TE-TM splitting and anisotropic splitting become comparable, mixing of the branches breaks the reciprocity of the dispersion. This results in the formation of a pair of minima on the lowest dispersion surface at $(0, k_{\rm min}^{\pm})$ with $k_{\rm min}^{\pm} \neq 0$, symmetrically displaced along $k_y$. Approaching the critical angle increases the distance between these minima, $2|k_{\rm min}| = k_{\rm min}^{+} - k_{\rm min}^{-}$, reaching a maximum at the point corresponding to the crossing of the dispersion surfaces, as depicted in Figs. 3(b) and 3(c). The energy of the minima $\hbar\omega_{\rm min} = \hbar\omega(0, k_{\rm min}^{\pm})$ increases with $\theta$, see blue curve in Fig. 3(a).

The 4×4 matrix formalism allows one to reveal polarization properties of light in the microcavity structure. Figure 4(a) shows the reflectance dispersion of the structure at the $k_x = 0$ cross section for the $X$-polarized incident light. The four-component incident electric field vector in (6)

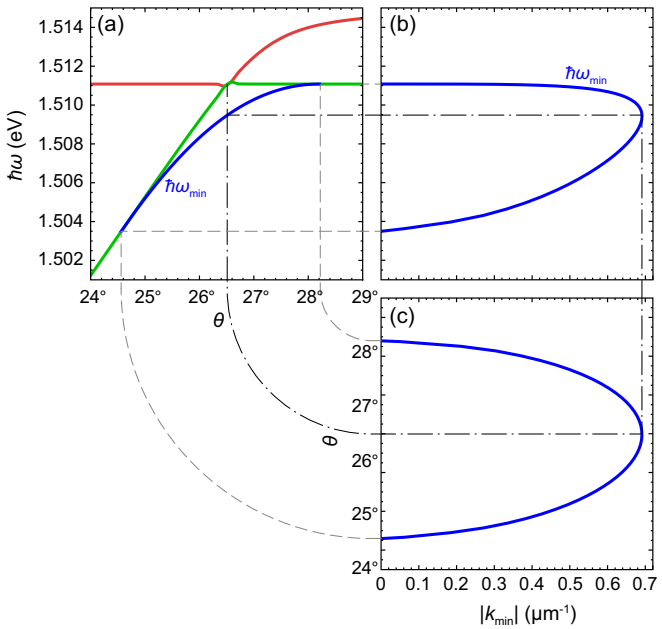


FIG. 3. (a) The dependencies of polariton energies $\hbar\omega(0,0)$ at the center ($k_{x,y}=0$) of the two lower dispersion surfaces (green and red) and the dependence of the energy minima $\hbar\omega_{\min}=\hbar\omega(0,|k_{\min}|)$ on the lowest dispersion surface (blue) on the rotation angle of LC molecules $\theta$. (b) Parametric dependence of the energy $\hbar\omega_{\min}$ on the absolute value of the wave number $|k_{\min}|$ of the minima of the lowest polariton dispersion branch. (c) The relationship between the wave number $|k_{\min}|$ and the angle $\theta$. Black dash-dotted lines link the parameters corresponding to the crossing of the two lowest dispersion surfaces at $(k_x,k_y)=0$. Gray dashed lines indicate the edges of the region with $|k_{\min}|\neq 0$. The parameters for the simulations are the same as those for Fig. 2(b).

then takes the form $\mathbf{E}_0=(1,0,E^p_{\leftarrow,0},E^s_{\leftarrow,0})^{\mathrm{T}}$. Since there is no reflected light at the output of the structure, the output field vector reduces to $\mathbf{E}_{N+1}=(E^s_{\rightarrow,N+1},E^s_{\rightarrow,N+1},0,0)^{\mathrm{T}}$. The circular polarization distribution of the reflected light found as $S_z=-2\mathrm{Im}[(E^p_{\leftarrow,0})^*E^s_{\leftarrow,0}]/(|E^p_{\leftarrow,0}|^2+|E^s_{\leftarrow,0}|^2)$ is shown in Fig. 4(b). It is evident that circular polarization is inherent to the eigenmodes of the system. Herewith, in each pair, different dispersion branches exhibit orthogonal circular polarizations, see blue (left) and red (right) distributions in Fig. 4(b). In the subsequent paragraphs, we will employ symmetry analysis to elucidate the underlying mechanisms that give rise to these peculiarities in the polariton dispersion of the considered structure.

### C. Symmetry analysis of the photon modes

The symmetry analysis allows us to establish the effective Hamiltonian underlying dispersion and reflectivity calculated in Sec. III B. It also helps predicting effects discussed below. The symmetry of the structure in the considered geometry is described by the $C_{2h}$ point group with the twofold rotation axis $C_2$ being the $y$ axis and horizontal reflection plane $\sigma_h\parallel(xz)$. This group also has an inversion center, i.e., the structure is symmetric with respect to $\mathbf{r}\rightarrow-\mathbf{r}$ transformation. There are four (vector) irreducible representations in this point group, summarized in Table I.

TABLE I. Irreducible representations of the $C_{2h}$ point group and examples of the basic functions. All representations are one dimensional. Sign + or − represents the parity of the functions with respect to the inversion.

| Representation | Functions |
|---|---|
| $A^+$ | $S_y, x^2, y^2, z^2, zx$ |
| $B^+$ | $S_x, S_z, xy, zy$ |
| $A^-$ | $y$ |
| $B^-$ | $x, z$ |

The multiplication rules are as follows:

$$A\otimes A=A,\quad B\otimes B=A,\quad A\otimes B=B, \tag{7}$$

with the natural parity multiplication rules: $+\otimes+=+$ and $+\otimes-=-$.

To establish the effective Hamiltonian we introduce the basic states for the electromagnetic field at the in-plane wave vector $\mathbf{k}=0$. We consider four relevant states with the polarization vectors $\hat{\mathbf{x}}$ and $\hat{\mathbf{y}}$ and the envelope functions of the field along the growth axis $f_1(z)$ and $f_2(z)$, where $f_1(z)$ is the even function of $z$ and $f_2(z)$ is the odd function. Numerical calculations of the polariton dispersion in Sec. III B as well as in Refs. [36,38,41] show that such states are indeed close in energy. The notations of the basic states and corresponding irreducible representations are as follows:

$$|x\rangle_1=\hat{\mathbf{x}}f_1(z),\quad \text{representation } B^-, \tag{8a}$$
$$|y\rangle_1=\hat{\mathbf{y}}f_1(z),\quad \text{representation } A^-, \tag{8b}$$
$$|x\rangle_2=\hat{\mathbf{x}}f_2(z),\quad \text{representation } A^+, \tag{8c}$$
$$|y\rangle_2=\hat{\mathbf{y}}f_2(z),\quad \text{representation } B^+. \tag{8d}$$

In the basis $(|x\rangle_1,|y\rangle_1,|x\rangle_2,|y\rangle_2)$ the effective Hamiltonian takes the form

$$\mathcal{H}_c(\mathbf{k})=\mathcal{H}_0(\mathbf{k})+\mathcal{H}_1(\mathbf{k}), \tag{9}$$

where $\mathcal{H}_0(\mathbf{k})$ is the $k^2$ Hamiltonian, which takes into account both parabolic dispersion, anisotropic splitting, and TE-TM splitting of the cavity modes. The latter effect results in the mixing of states with the same parity. As a result, $\mathcal{H}_0(\mathbf{k})$ takes the form

$$\mathcal{H}_0(\mathbf{k})=\begin{pmatrix} E_{x,1}(\mathbf{k}) & E_{xy,1}(\mathbf{k}) & 0 & 0\\ E_{xy,1}(\mathbf{k}) & E_{y,1}(\mathbf{k}) & 0 & 0\\ 0 & 0 & E_{x,2}(\mathbf{k}) & E_{xy,2}(\mathbf{k})\\ 0 & 0 & E_{xy,2}(\mathbf{k}) & E_{y,2}(\mathbf{k})\end{pmatrix}, \tag{10}$$

with

$$E_{a,b}(\mathbf{k})=E_{a,b}+\frac{\hbar^2k_x^2}{2m_{xx}^{(ab)}}+\frac{\hbar^2k_y^2}{2m_{yy}^{(ab)}}, \tag{11}$$

$$E_{xy,b}(\mathbf{k})=\frac{\hbar^2k_xk_y}{2m_{xy}^{(b)}}, \tag{12}$$

where the subscripts $a=x,y$ and $b=1,2$, so the pair $(a,b)$ denotes the basic state in Eq. (8). $m_{xx}^{(ab)}$, $m_{yy}^{(ab)}$ are the effective

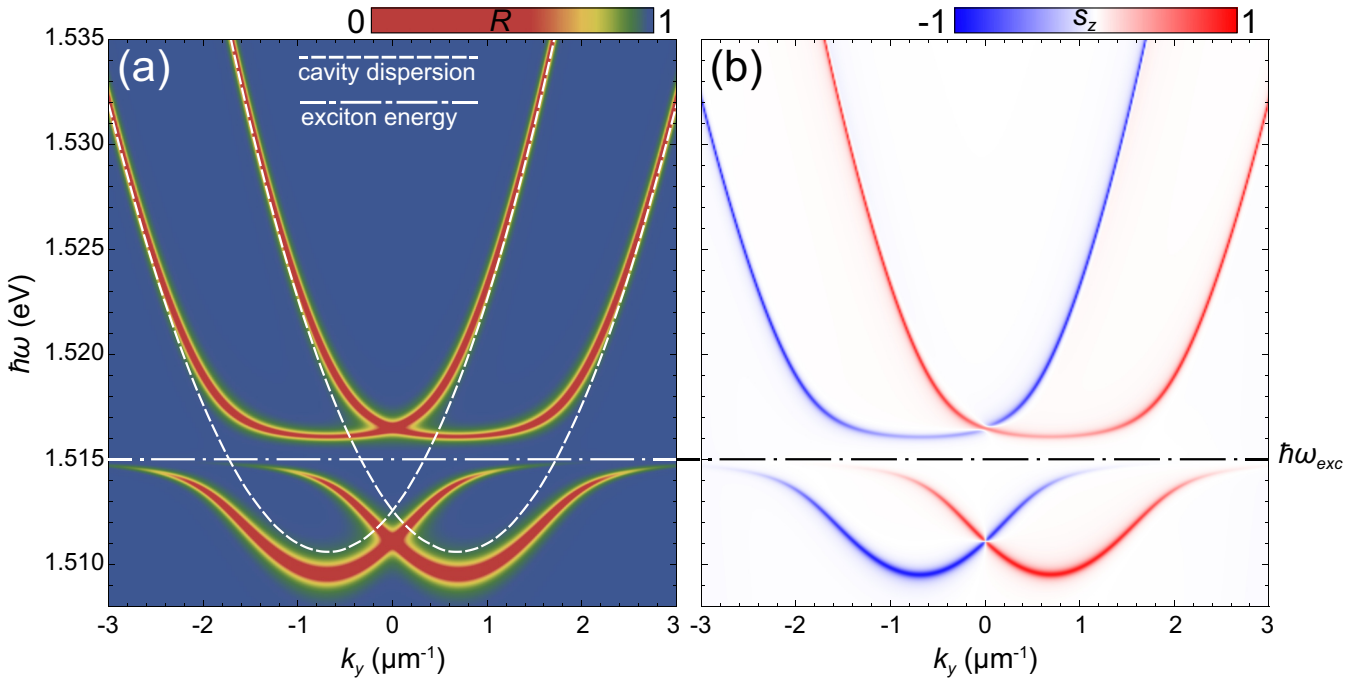


FIG. 4. (a) Reflectance spectrum of the polariton LC cavity structure at $k_x = 0$. (b) Circular polarization degree of the reflected light at the linear polarization of the incident light. Blue (left) and red (right) dispersion branches exhibit orthogonal circular polarizations. The parameters for simulations are the same as for Fig. 2(b). The dashed curve and the dash-dotted line indicate the cavity dispersion without the exciton resonance and the QW exciton energy, respectively.

masses of the photonic modes, and $m_{xy}^{(b)}$ describes the TE-TM splitting of the modes. The term $\mathcal{H}_1(\mathbf{k})$ describes $\mathbf{k}$-linear mixing of the states and takes the form

$$\mathcal{H}_1(\mathbf{k}) = \begin{pmatrix} 0 & 0 & \mathrm{i}\beta_x k_x & \mathrm{i}\alpha' k_y \\ 0 & 0 & \mathrm{i}\alpha k_y & \mathrm{i}\beta_y k_x \\ -\mathrm{i}\beta_x k_x & -\mathrm{i}\alpha k_y & 0 & 0 \\ -\mathrm{i}\alpha' k_y & -\mathrm{i}\beta_y k_x & 0 & 0 \end{pmatrix}. \tag{13}$$

Note that the $\mathbf{k}$-linear mixing of the states of different parity is possible in the centrosymmetric structures. This is in stark contrast with $\mathbf{k}$-linear spin-dependent terms in electronic spectrum where the Bloch functions have the same parity (i.e., the conduction band is described by a single orbital Bloch function) and the linear-in-wave-vector terms are allowed only for the structures lacking an inversion center, i.e., being noninvariant under $\mathbf{r} \to -\mathbf{r}$ transformation.

In Refs. [36,41] the situation where the states $|x\rangle_2$ and $|y\rangle_1$ are close in energy, $E_{x,2} \approx E_{y,1}$, while the other states are far has been studied. In this situation only the inner $2\times2$ block of the Hamiltonian $\mathcal{H}(\mathbf{k})$ is relevant with the result

$$\mathcal{H}_{\mathrm{c},2\times2} = \begin{pmatrix} E_{y,1}(\mathbf{k}) & \mathrm{i}\alpha k_y \\ -\mathrm{i}\alpha k_y & E_{x,2}(\mathbf{k}) \end{pmatrix}. \tag{14}$$

Equation (14) can be brought to the form of Eq. (1) of Ref. [36] if we change the basis from $|x\rangle_2$ and $|y\rangle_1$ to the "circular" states $(|x\rangle_2 \pm \mathrm{i}|y\rangle_1)/\sqrt{2}$ and disregard the differences of the effective masses for the states 1 and 2,

$$\tilde{\mathcal{H}}_{\mathrm{c},2\times2} = \frac{\hbar^2 k_x^2}{2m_{xx}} + \frac{\hbar^2 k_y^2}{2m_{yy}} + \alpha\hat{\sigma}_z k_y + \frac{E_{x,2} - E_{y,1}}{2}\hat{\sigma}_x. \tag{15}$$

We stress that the $2\times2$ Hamiltonian describes the mixing of the states with different parity. Although it resembles the famous spin-orbit terms of Rashba and Dresselhaus (structure or bulk inversion asymmetry) in semiconductors [51–55], the observed polariton behavior in our centrosymmetric microcavity emerges from the distinct interaction dynamics within the cavity, modulated by the anisotropic properties of the LC medium, rather than structure's symmetry reduction or gyrotropy.

### D. Light-matter coupling in the LC-filled optical microcavity

Having addressed the spectrum of an empty cavity, we now turn to the description of the exciton-polariton modes in the presence of the active layers. We consider two QWs placed at the coordinates $z_1$ and $z_2$ in the cavity layer. In each QW we consider a radiative doublet of excitonic states. The Hamiltonian describing each radiative doublet $\mathcal{H}_{\mathrm{exc},i}$ $(i = 1, 2)$ takes a simple form

$$\mathcal{H}_{\mathrm{exc},i} = \begin{pmatrix} E_{\mathrm{exc},x,i} + \frac{\hbar^2 k^2}{2m_{\mathrm{exc},i}} & 0 \\ 0 & E_{\mathrm{exc},y,i} + \frac{\hbar^2 k^2}{2m_{\mathrm{exc},i}} \end{pmatrix}, \tag{16}$$

where the difference of the energies $E_{\mathrm{exc},x,i} - E_{\mathrm{exc},y,i}$ is related to the anisotropic splitting of the exciton radiative doublet in $(xy)$ axes induced by the strain and interface anisotropy, $m_{\mathrm{exc},i}$ is the exciton effective mass in the $i$th QW, and $\mathbf{k}$ is its in-plane wave vector.

The interaction of an exciton with a given photonic mode is described by the product $V_i f_j(z_i)$ where $f_j$ is the envelope function of the field introduced in Eqs. (8) and $V_i$ is the

TABLE II. Values of the parameters in the Hamiltonian (19) used for fitting the dispersion of eigenmodes of the LC-filled microcavity in Figs. 2(b) and 7(b). $m_e$ is the free electron mass.

| Quantity | Units | Fig. 2(b) | Fig. 7(b) |
|---|---|---|---|
| $E_{y,1}$ | eV | 1.5126 | 1.5111 |
| $E_{x,2}$ | eV | 1.5126 | 1.5123 |
| $V$ | meV | 2.4 | 2.16 |
| $\alpha$ | meV μm | 5.8 | 4 |
| $m_{xx}^{(y1)}$ | $10^{-5}m_e$ | 0.86 | 0.79 |
| $m_{yy}^{(y1)}$ | $10^{-5}m_e$ | 1.13 | 0.71 |
| $m_{xx}^{(x2)}$ | $10^{-5}m_e$ | 0.78 | 0.76 |
| $m_{yy}^{(x2)}$ | $10^{-5}m_e$ | 0.74 | 1.03 |

coupling constant depending on the material parameters. As a result, the total 8×8 Hamiltonian describing two QWs in a microcavity reads

$$\mathcal{H} = \begin{pmatrix} \mathcal{H}_{\mathrm{exc},1} & \hat{0} & \mathcal{V}^{(1)} \\ \hat{0} & \mathcal{H}_{\mathrm{exc},2} & \mathcal{V}^{(2)} \\ \mathcal{V}^{(1),\dagger} & \mathcal{V}^{(2),\dagger} & \mathcal{H}_{\mathrm{c}} \end{pmatrix}, \tag{17}$$

where the 4×2 matrices $\mathcal{V}^{(i)}$ describe the light-matter interaction as

$$\mathcal{V}^{(i)} = \begin{pmatrix} V_i f_1(z_i) & 0 & V_i f_2(z_i) & 0 \\ 0 & V_i f_1(z_i) & 0 & V_i f_2(z_i) \end{pmatrix}. \tag{18}$$

If QWs take symmetric positions with respect to the microcavity center, then $z_2 = -z_1$, $f_1(z_1) = f_1(z_2)$ and $f_2(z_1) = -f_2(z_2)$. In particular case where both QWs are in the cavity center, $z_{1,2} = 0$, coupling with the mode 2 vanishes. Similar situation has been analyzed, within a simplified Hamiltonian for a cavity, in Ref. [38].

The Hamiltonian (17) for describing the polariton states characterized by the dispersion in Fig. 2, can be reduced to a 4×4 matrix as following:

$$\mathcal{H}_{\mathrm{I}} = \begin{pmatrix} \mathcal{H}_{c,2\times2} & V\hat{\sigma}_0 \\ V\hat{\sigma}_0 & E_{\mathrm{exc}}\hat{\sigma}_0 \end{pmatrix}, \tag{19}$$

where $V$ is the exciton-photon interaction constant, which is equal for both photonic modes. We also neglect anisotropy of QWs and assume the exciton effective mass infinitely large taking the exciton energy constant $E_{\mathrm{exc}}$. Eigenvalues of the Hamiltonian (19) in comparison with the MF calculations are shown in the side wall plots in Fig. 2. Very good agreement of the two approaches is seen. Values of the parameters used for fitting are given in Table II.

## IV. POLARITON PROPAGATION IN THE LC-FILLED CAVITY

The nonreciprocal dispersion and peculiar polarization properties of the polariton eigenmodes of the structure give rise to distinct optical effects. To reveal these effects, we conduct a series of numerical experiments simulating the passage of a cw laser beam through the considered structure. We solve Maxwell's equations using the 4×4 MF for the incident beam of a Gaussian shape $\mathbf{E}_0 \propto \exp[-\mathbf{r}^2/2w^2]\exp[i(\mathbf{k}_0\mathbf{r} - \omega_0 t)]\mathbf{p}_0$ of width $w$, where $\mathbf{r} = (x, y)$ is the in-plane coordinate. The in-plane wave vector $\mathbf{k}_0$ and the frequency $\omega_0$ of the beam are chosen with the intention of being close to the polariton dispersion surface (Fig. 2), thereby exciting the polariton eigenmodes of the structure. The vector $\mathbf{p}_0$ is responsible for the polarization of the incident beam in the XY basis, $\mathbf{p}_0 = (p_X, p_Y)^{\mathrm{T}}$, the absolute value of $\mathbf{p}_0$ describes the peak field of the beam.

In the structure under consideration, losses are primarily due to photonic losses, which occur as photons escape through the mirrors, and nonradiative losses associated with absorption in the excitonic layer. The high refractive index contrast in DBRs effectively minimizes photonic losses. This, coupled with the low excitonic losses in the selected QW material, ensures a robust localization of polariton modes within the microcavity. Consequently, this allows the polariton modes to occupy extensive areas in the plane of the microcavity, enabling them to cover distances ranging from tens to hundreds of micrometers from the point of injection. This extended reach enables the manifestation of various spin/polarization spatial effects. Figures 5 and 6 illustrate several examples of the effects reproduced by us numerically and discussed below.

We analyze the intensity distribution $I(\mathbf{r}) = |E_{x,j}(\mathbf{r})|^2 + |E_{y,j}(\mathbf{r})|^2$ and polarization of the photon field at the boundary of the top DBR and the LC-filled cavity layer. The Stokes vector components are used for characterizing the distribution of the linear, $S_x(\mathbf{r}) = (|E_{x,j}(\mathbf{r})|^2 - |E_{y,j}(\mathbf{r})|^2)/I(\mathbf{r})$, diagonal/antidiagonal, $S_y(\mathbf{r}) = 2\mathrm{Re}[E_{x,j}(\mathbf{r})E_{y,j}^*(\mathbf{r})]/I(\mathbf{r})$, and circular, $S_z(\mathbf{r}) = -2\mathrm{Im}[E_{x,j}(\mathbf{r})E_{y,j}^*(\mathbf{r})]/I(\mathbf{r})$, polarizations. The intensity distribution in $k$ space $I(\mathbf{k})$ is also the focus of our attention.

### A. Birefringence of polaritons

In the first numerical experiment illustrated in Figs. 5(a)–5(e), we focus on the behavior of a polariton wave packet excited by a linearly polarized laser beam that is resonant with both lower polariton dispersion branches at their crossing point ($k_{0,y} = 0$ and $k_{0,x} \neq 0$). Specifically, we set $k_{0,x} = 0.6\,\mu\mathrm{m}^{-1}$ and $\hbar\omega_0 \approx 1.512\,\mathrm{eV}$. The excitation conditions are marked by a red six-pointed star in Fig. 2(b). Also see Fig. 5(e) to correlate the excitation conditions with the shape of the polariton dispersion contours. The incident beam has a width of 10 μm. The density distribution shown in Fig. 5(a) reveals that the polariton wave packet exhibits birefringence within the microcavity plane. This birefringence is accompanied by the spatial separation of polaritons with opposite circular polarizations, as shown in Fig. 5(d). Linear polarization is manifested near the entry point of the incident beam, replicating the polarization of the latter, see Fig. 5(b). Away from the incidence spot, the presence of the linear and diagonal components [Figs. 5(b) and 5(c)] is significantly diminished due to the dominance of the circular polarization. This behavior is reminiscent of the optical Stern-Gerlach experiment [56], including a similar phenomenon observed in LC-filled microcavities without the strong light-matter coupling [37].

In Figs. 5(f)–5(j), we explore a different scenario by keeping $\hbar\omega_0$ and setting $k_{0,x} = k_{0,y} = 0$, which shifts the incident beam away from resonance with the polariton modes

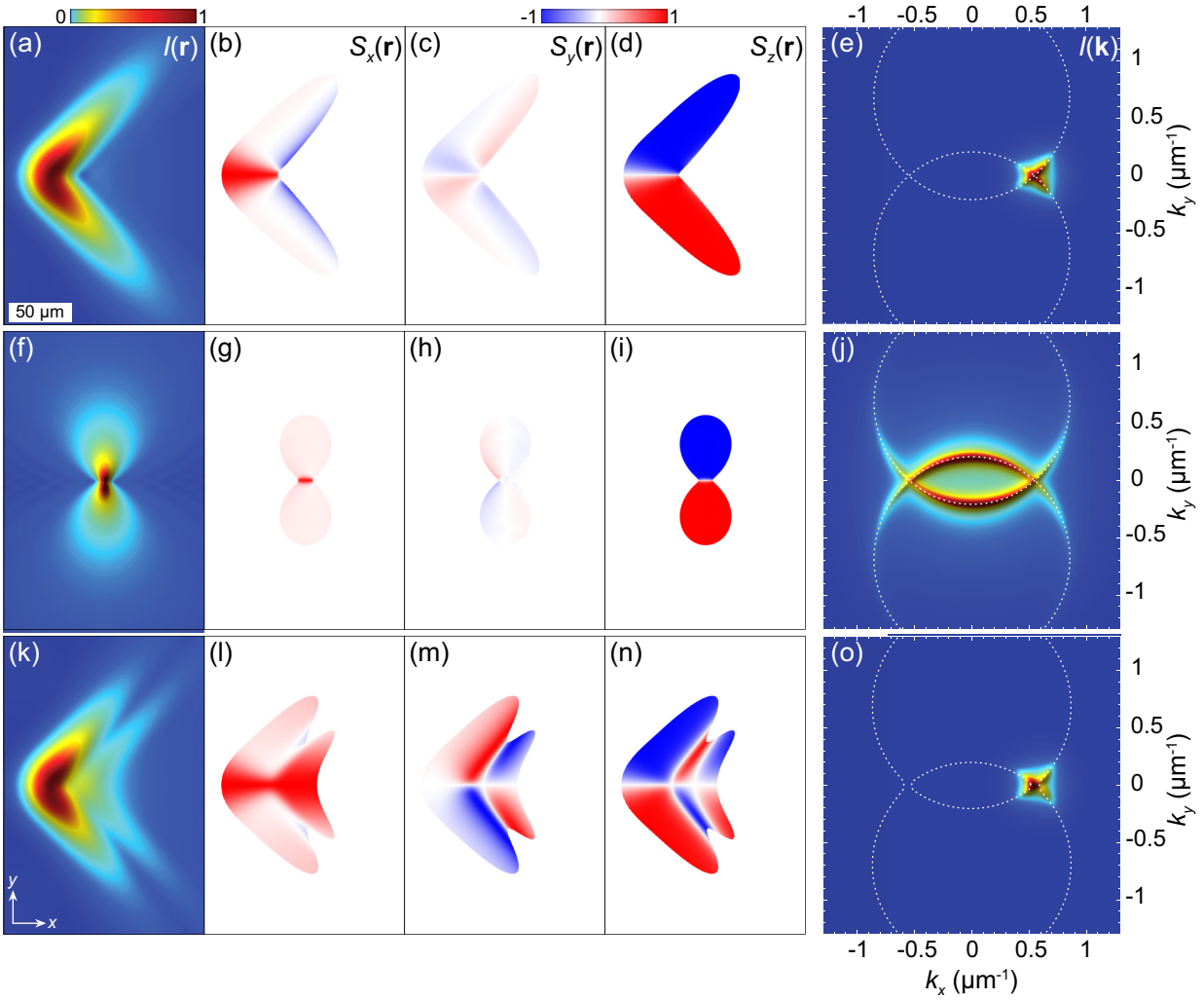


FIG. 5. Polariton propagation in the LC-filled microcavity with embedded QWs. From left to right: Spatial distribution of the intensity $I(\mathbf{r})$ and polarization components $S_{x,y,z}(\mathbf{r})$, as well as distribution in $k$ space $I(\mathbf{k})$ at the boundary of the top DBR and the cavity layer of the polariton states excited by the inclined Gaussian beams. The parameters of excitation are following: $k_x = 0.6\,\mu\text{m}^{-1}$, $w = 10\,\mu\text{m}$, $\theta \approx 26.52^\circ$ (a)–(e), $k_x = 0$, $w = 2.5\,\mu\text{m}$, $\theta \approx 26.52^\circ$ (f)–(j), and $k_x = 0.6\,\mu\text{m}^{-1}$, $w = 10\,\mu\text{m}$, $\theta = 26.45^\circ$ (k)–(o). For all panels, $\hbar\omega = 1.512\,\text{eV}$ and $k_y = 0$. The other parameters are the same as for Fig. 2(b). White dotted lines in the rightmost panels are guides for the eyes corresponding to the cross section of the polariton dispersion at $\hbar\omega = 1.512\,\text{eV}$. The polarization of the incident beam is taken linear, $\mathbf{p}_0 = (1, 0)^\text{T}$.

[indicated by red five-pointed stars in Fig. 2(b)]. In order to still excite polaritons under these conditions, we significantly broaden the spectrum of the beam by reducing its width to $w = 2.5\,\mu\text{m}$. As a result, we observe a symmetric butterfly-like pattern in the polariton density distribution, as shown in Fig. 5(f). This pattern arises from the occupation of orthogonally polarized polariton dispersions around the crossing region [Fig. 5(i)]. In such excitation conditions, linear [Fig. 5(g)] and diagonal [Fig. 5(h)] polarization components are also weakly expressed. The polariton density distribution in $k$ space highlights the cross section of the polariton dispersion in Fig. 5(j).

In the numerical experiment illustrated in Figs. 5(k)–5(o), we slightly change the angle $\theta$ of the LC molecules to avoid crossing of the polariton dispersion branches. The other parameters are taken the same as for the first numerical experiment. This action results in the emergence of the jellyfish-like polariton density pattern, Fig. 5(k). The gap between the dispersion branches in $k$ space [cf. the guides for the eye in Figs. 5(e) and 5(o)] results in the emergence of the polariton density and polarization domains in the microcavity plane, see Figs. 5(k) and 5(l)–5(n), respectively. It is noteworthy that within the domains, the magnitudes of the diagonal $|S_y(\mathbf{r})|$ and circular $|S_z(\mathbf{r})|$ polarization degrees are shifted in the cavity plane with respect to each other such that the maximum of the former coincides with the minimum of the latter, cf. Figs. 5(m) and 5(n).

The emergence of density and polarization domains in our system is fundamentally attributed to the interplay between the anisotropic splitting, induced in the LC-filled layer, and the spatial distribution of the exciton-polariton modes within the microcavity. When the dispersion branches exhibit a gap in $k$ space, indicative of an energy separation for polaritons with orthogonal polarizations, it leads to distinct propagation characteristics for these modes. This energy disparity, and the consequent difference in effective masses for polaritons

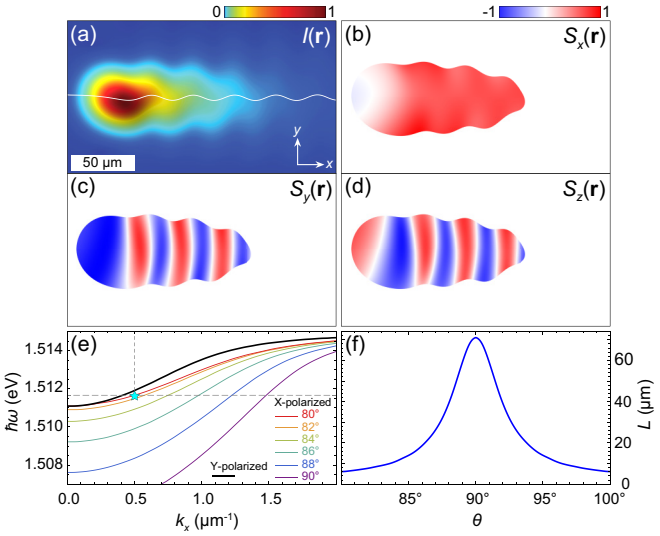


FIG. 6. *Zitterbewegung* of exciton polaritons. Distribution of the intensity $I(\mathbf{r})$ (a) and polarization components $S_{x,y,z}(\mathbf{r})$ (b)–(d) of the polariton wave packet under cw pump. White curve in (a) shows the center-of-mass trajectory of polaritons. The orientation angle of the LC molecules $\theta$ is taken 88°. (e) Dispersion of the X- and Y-polarized cavity modes at different orientation of the LC molecules $\theta$. (f) The change of the period of the *zitterbewegung* with changing angle $\theta$. The energy and wave vector of the excitation beam used for simulations in (a)–(d) are indicated by the cyan star marker in (e). The excitation is taken resonant to the X-polarized mode at $\theta = 90°$. All parameter of the structure except the angle $\theta$ are the same as for Fig. 5.

with orthogonal polarizations, results in variations in group velocity and diffusion rates across $k$ space. Consequently, when a polariton wave packet is generated within the cavity and partially overlaps in momentum space with both dispersion branches, it spatially evolves into distinct regions where polaritons of one polarization are more concentrated than those of the other. This separation effectively manifests as the observed density domains.

### B. *Zitterbewegung*

When the LC molecules are aligned along the direction of structure growth ($\theta = 90°$), the microcavity is isotropic in the $xy$ plane. The dominating polarization optical effect in this case is the TE-TM splitting, which mixes polariton modes of the same parity [57]. In the case of the cw resonant incident light beam, the TE-TM splitting is known to cause the *zitterbewegung* of polaritons [21–23]. The *zitterbeweging* is known for systems characterized by split kinetic energy dispersion branches and consisting of oscillations of the polariton trajectory in the direction normal to the propagation direction.

The photonic contribution to the TE-TM splitting is dominant and is characterized by the off-diagonal terms $E_{xy,b}(\mathbf{k})$ in (10). The period of the *zitterbewegung* is determined by the total splitting of the modes, which can be controlled. To enhance or reduce the magnitude of the *zitterbewegung*, the TE-TM splitting can be supplemented with additional anisotropic splitting in linear polarizations. In a previous study [22], the anisotropy was introduced via the excitonic fraction by applying an external magnetic field in the Voigt geometry to split the QW exciton states. In contrast, here additional anisotropy can be introduced through the photonic component by rotating the LC molecules relative to the microcavity plane. By slightly changing $\theta$ with respect to the structure growth axis, we can modify the magnitude of the total splitting while maintaining the TE-TM splitting as the dominant effect. Figures 6(a)–6(d) depict the spatial distribution of the density and polarization components of the polariton wave packet in the presence of the *zitterbewegung*. It is notable that the trembling motion of the center of mass of the polariton wave packet is accompanied by oscillations of the circular polarization degree, cf. Ref. [58] for similar effect in electronic systems. This phenomenon can be understood by considering the wave packet as a superposition of TE and TM polarized states with slightly different wave vectors. As the wave packet evolves within the microcavity, the phase difference between these components changes, leading to oscillations in the overall polarization state.

Figure 6(e) illustrates the dispersions of the split polariton branches at different angles $\theta$. It can be observed that the dispersion of the $Y$-polarized mode remains unchanged as $\theta$ varies, while the dispersion of the $X$-polarized mode shifts to lower energy as the LC molecule axis deviates from the structure growth axis. Consequently, as $\theta$ deviates from 90°, the splitting of the polariton modes increases.

Figure 6(f) shows the variation of the period of the *zitterbewegung*, denoted as $L$, with changing angle $\theta$, while keeping the wave number $k_{0,x}$ constant. The maximum period occurs at $\theta = 90°$ when only the TE-TM splitting is present. As the deviation of $\theta$ increases, the period decreases. It is important to note that the increase in the splitting magnitude leads to a decrease in the amplitude of the *zitterbewegung* and contributes to the damping of the oscillations, ultimately reducing the observability of the effect.

## V. PHOTON-POLARITON MIXING

Let us now turn our attention to the structure depicted schematically in Fig. 7(a). In contrast to the structure shown in Fig. 1(a), this configuration includes a single QW located at the center of the cavity layer. To prevent direct contact between the QW and the LC, we have introduced two protective $SiO_2$ layers on both sides of the QW. As shown in panel (b) of Fig. 7, the coupling with the exciton layer only occurs for the even cavity mode, while the odd mode remains purely photonic. Thus, the structural anisotropy induced by the LC-filled cavity layer leads to the mixing between photonic and polaritonic modes. The dispersion of the three eigenmodes of the structure, calculated using MF, is presented in Fig. 7(c). For the specific parameters employed (including the angle $\theta$), the dispersions of the two lower modes exhibit crossing around $(k_x, k_y) = (0, 0)$ and their dependence on $k_x$ is linear. This region of interest is magnified in Fig. 8(a).

Amending the angle $\theta$, we obtain two tilted Dirac cones at $(k_x, k_y) = (0, k_{y,D})$, see Fig. 8(b). The Hamiltonian for the system reduces, in agreement with Ref. [38] to

$$\mathcal{H}_{\mathrm{II}} = \begin{pmatrix} \mathcal{H}_{c,2\times2} & \tilde{V}^{\dagger} \\ \tilde{V} & E_{\mathrm{exc}} \end{pmatrix}, \tag{20}$$

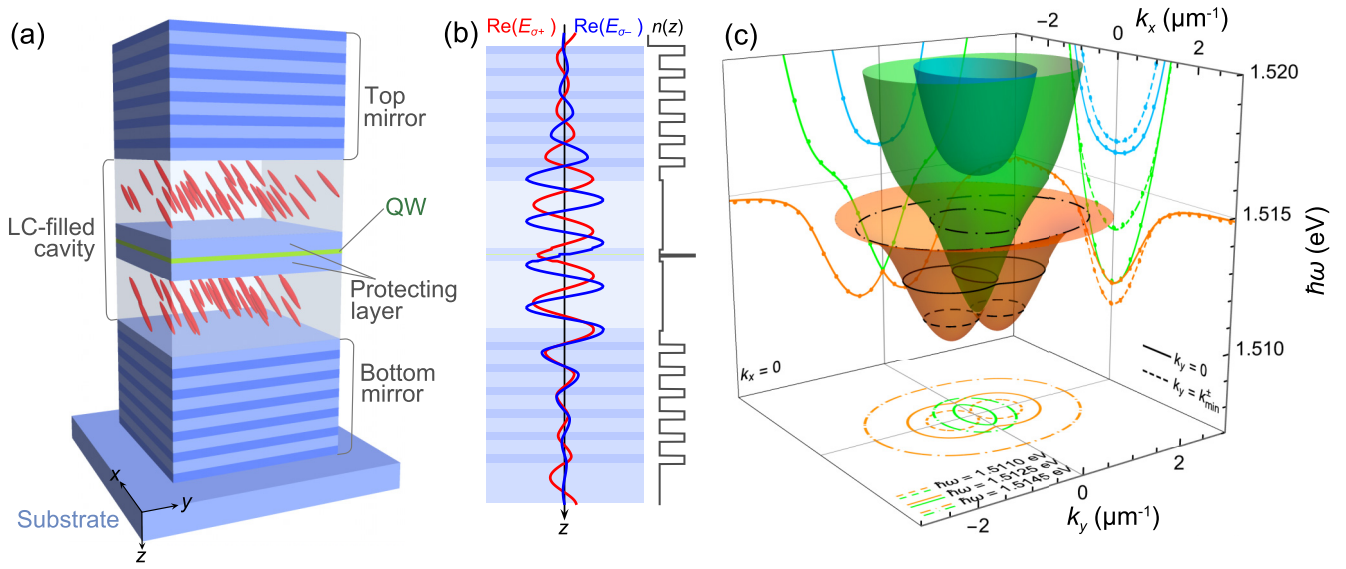


FIG. 7. Same as in Fig. 1 (a), (b) and in Fig. 2 (c) but for the LC-filled microcavity with a single QW. The angle $\theta$ is taken 16.59°. The thickness of each LC-filled cavity sublayer is $d/2 = 0.7\,\mu$m.

where $\tilde{V} = (V, 0)$. Eigenvalues of the Hamiltonian (20) in comparison with the MF calculations are shown in the side wall plots in Fig. 7(c). Values of the parameters used for fitting are given in Table II.

The dependencies of the characteristic points of the two lower dispersion surfaces on the orientation of the LC molecules characterized by the angle $\theta$ are illustrated in Fig. 9. Similar to the scenario depicted in Fig. 3, anisotropic splitting acts as the mechanism for the mixing of dispersion branches. This mixing is particularly noticeable near a certain angle $\theta$ (estimated as approximately 16.59° for the considered geometry), at which the splitting is significant enough to stand out against TE-TM splitting, yet sufficiently modest to allow for the mutual influence of the split resonant modes. The mixing results in the formation of two symmetrically positioned minima along $k_y$ on the lowest dispersion surface at $(0, k_{\rm min}^{\pm})$, see blue curves in Fig. 9.

The key distinction from the previously discussed case lies in the fact that the two lower dispersion branches undergo crossing not only at the critical angle $\theta$ and not just at $(k_x, k_y) = (0, 0)$. As one moves away from the critical angle, the positions of the crossing points $\hbar\omega_{\rm D} = \hbar\omega(k_{\rm D}^{\pm}, 0)$ diverge from the center of the dispersion surface, symmetrically along the $k_x$ axis. At these crossing points also referred to as

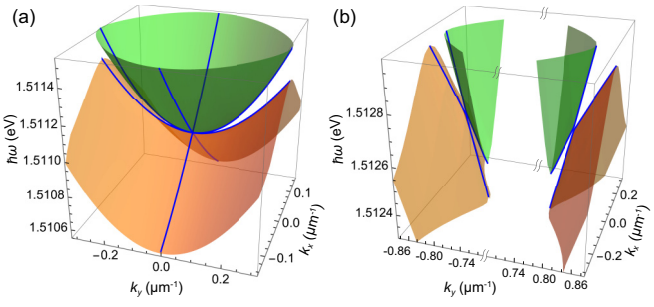


FIG. 8. Magnified dispersion regions around the positions of crossing of the two lowest dispersion branches. Around $(k_x, k_y) = (0, 0)$ at $\theta \approx 16.59°$ (a) and around $(k_x, k_y) = (0, k_{y,D}) \approx (0, \pm 0.8)$ at $\theta \approx 16.1°$ (b).

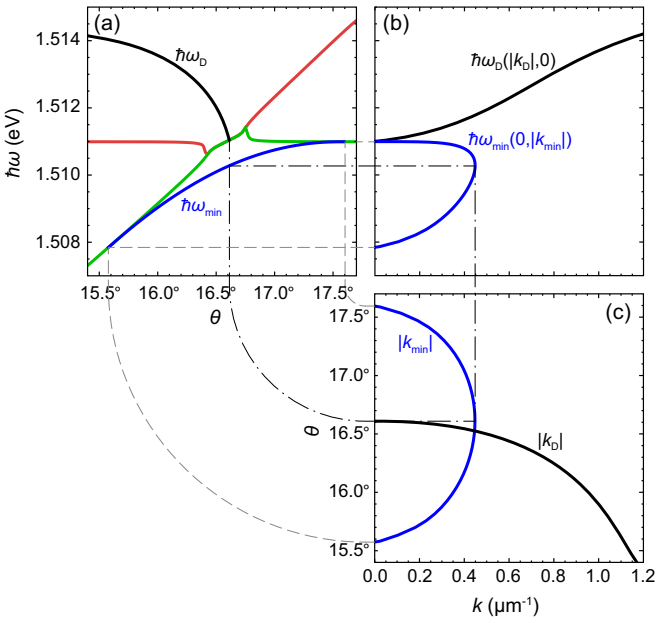


FIG. 9. (a) The dependencies of polariton energies $\hbar\omega(0, 0)$ at the center ($k_{x,y} = 0$) of the two lower dispersion surfaces (green and red), the dependence of the energy $\hbar\omega_{\rm D} = \hbar\omega(|k_{\rm D}|, 0)$ of crossing of the dispersion surfaces (black), and the dependence of the energy minima $\hbar\omega_{\rm min} = \hbar\omega(0, |k_{\rm min}|)$ on the lowest dispersion surface (blue) on the rotation angle of LC molecules $\theta$. (b) Parametric dependence of the energies $\hbar\omega_{\rm min}$ and $\hbar\omega_{\rm D}$ on $|k_{\rm min}|$ and $|k_{\rm D}|$, respectively. (c) The relationships between the wave numbers $|k_{\rm min,\,D}|$ and the angle $\theta$. Black dash-dotted lines link the parameters corresponding to the crossing of the two lowest dispersion surfaces at $(k_x, k_y) = 0$. Gray-dashed lines indicate the edges of the region with $|k_{\rm min}| \neq 0$. The parameters for the simulations are the same as those for Fig. 7(c).

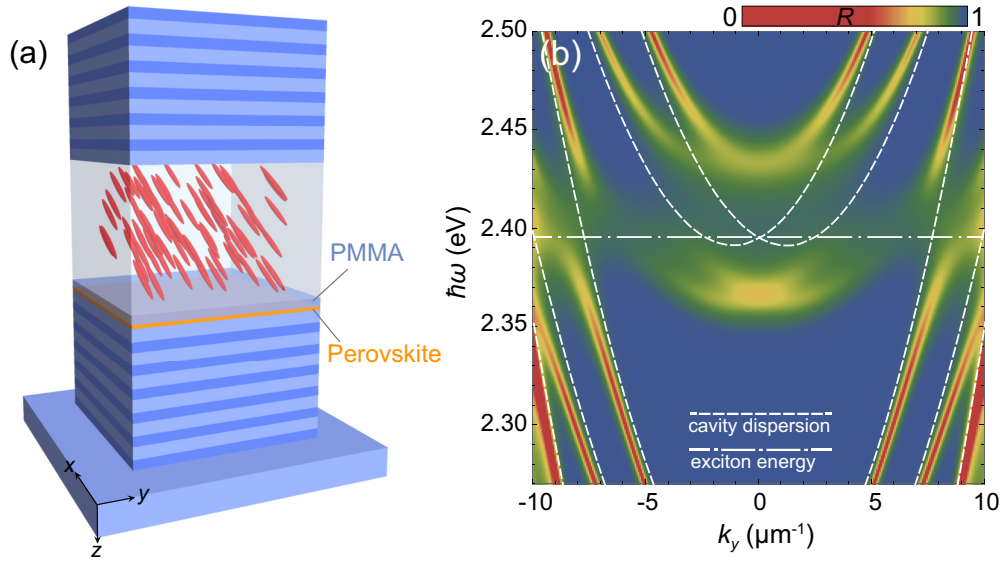


FIG. 10. LC-filled microcavity with an embedded perovskite layer. (a) Schematic of the structure. (b) Reflectance spectrum at $k_x = 0$. The dashed curve and the dash-dotted line indicate the cavity dispersion without the exciton resonance and the exciton energy, respectively.

diabolical points, the anticipated tilted Dirac cones are observed, as introduced in Fig. 8(b) and depicted by the black curves in Fig. 9. It is noteworthy that diabolic points are only observed at angles $\theta$ that do not exceed the critical angle. This is due to the fact that further increasing the angle causes the initially converging split branches to start diverging.

## VI. STRUCTURE WITH A PEROVSKITE LAYER

Considerable attention has been given to structures incorporating a two-dimensional perovskite layer into a microcavity layer due to the large binding energy of perovskite excitons, which enables strong exciton-photon coupling even at room temperature [11,39]. In this context, we now examine a microcavity structure where QWs are replaced with a perovskite layer, as illustrated in Fig. 10(a). Following the approach in [39], we consider a polycrystalline two-dimensional (2D) phenylethylammonium iodide perovskite $(C_6H_5C_2H_4NH_3)_2PbI_4$ (PEPI) characterized by the dielectric function

$$\varepsilon_{\mathrm{PEPI}} = \varepsilon_0 + \frac{f}{E_{\mathrm{exc}}^2 - (\hbar\omega)^2 - i\hbar^2\gamma\omega}, \tag{21}$$

where $\varepsilon_0 = 4.107$, $f = 0.712\,\mathrm{eV}^2$, $\hbar\gamma = 40.4$ meV, and $E_{\mathrm{exc}} = 2.395\,\mathrm{eV}$. Note that by contrast to (2), here we use the dielectric function with nonresonant contributions, but their account does not change the results significantly since $\hbar\gamma \ll E_{\mathrm{exc}}$. We use only one layer of thickness of 20 nm adjacent to the bottom mirror and covered by PMMA layer of thickness of 30 nm, see Fig. 10(a).

Figure 10(b) shows the reflectivity spectrum of the structure at the resonance of the perovskite excitons with both cavity modes at $\mathbf{k} = 0$. The following peculiarities of the dispersion of the structure eigenmodes can be seen. First, the strong light-matter coupling still takes place in the structure resulting in the avoided crossing of the polariton dispersion branches. Second, the splitting between the upper and lower polariton branches is large compared to Fig. 4 and is estimated as about 65 meV. Third, cavity modes that extend from the exciton resonance contribute to the exciton-photon coupling in the structure. In Fig. 10(b), the dispersions of such modes are pronounced at $|k_y| > 5\,\mu\mathrm{m}^{-1}$. This becomes possible since the Rabi splitting approaches the splitting of the cavity modes. Thus the Hamiltonian for the structure cannot be reduced to the 4×4 matrix form. Last, but not least, despite the strong coupling, the polariton line turns out to be extremely broad due to high losses in the perovskite layer. This limits the spread of polaritons in the microcavity plane to a few microns and hampers observation of any propagation-related spin and polarization effects in such structures.

## VII. CONCLUSIONS

In conclusion, here we presented the results of the theoretical investigation of optical microcavities filled with liquid crystal media containing embedded quantum wells. What sets liquid crystal filled microcavities apart is their exceptional ability to manipulate the polarization characteristics of the photonic fraction of polariton states through the external influence on liquid crystal molecule orientation. This remarkable control opens up possibilities for realizing controllable synthetic Hamiltonians tailored to the microcavity polariton eigenmodes, exemplified by those incorporating Rashba and Dresselhaus spin-orbit terms. The tailored Hamiltonians potentially facilitate the study of complex quantum phenomena like the anomalous Hall effect and topological insulators in a simplified, controllable environment. They provide a streamlined yet effective platform for delving into complex quantum states and behaviors, enabling advancements in optoelectronic, and spintronic device applications.

The controllability of the polarization characteristics can be further extended to the controllability of the orbital variable of exciton polaritons through the mechanisms of the spin-orbit interaction, resulting in various spin-dependent propagation

effects. Through our numerical experiments, we have successfully reproduced and investigated phenomena such as birefringence and *zitterbewegung* of exciton polaritons. These findings highlight the potential of liquid crystal filled microcavities as platforms for the manipulation and study of polariton states with unique spatial characteristics.

We have introduced a distinct microcavity geometry designed to facilitate spin-orbit coupling between purely photonic and polaritonic modes within the cavity. This geometry relies on leveraging liquid crystal induced optical anisotropy to ensure resonance between orthogonally polarized even and odd cavity modes, while placing the exciton layer at the center of the cavity layer maximizes the coupling with the former and minimizes it with the latter. In this geometry, we successfully demonstrated the formation of tilted Dirac cones in a dispersion of bosonic system. This achievement is noteworthy for its implications in directional photon manipulation and the dynamic tuning of photonic states, enabled by the adjustable liquid crystal environment. The ability to control these features not only broadens the understanding of Dirac materials but also opens up practical avenues for designing photonic devices with customizable dispersion properties. Specifically, this includes the development of directional light propagation devices and systems exhibiting directional nonlinearity.

Finally, we investigated the effects of the incorporation of a two-dimensional perovskite layer into the microcavity structure. Although the strong light-matter coupling still takes place in such structure, the significant linewidth of the polaritons due to high losses in the perovskite layer limits their spread in the microcavity plane, making the observation of spin-dependent propagation effects more challenging.

## ACKNOWLEDGMENTS

The support of Saint-Petersburg State University (research Grant No. 122040800257-5) and the state assignment in the field of scientific activity of the Ministry of Science and Higher Education of the Russian Federation (theme FZUN-2020-0013, state assignment of VlSU) are acknowledged. Work of M.M.G. was supported by the RSF Project No. 23-12-00142 (symmetry analysis and analytical light-matter coupling theory).

## APPENDIX: DETERMINATION OF PROPAGATION CONSTANTS WITHIN THE 4×4 MATRIX FORMALISM

The 4×4 MF is used for revealing propagation of electromagnetic waves in stratified media composed of homogeneous layers with different optical properties. The formalism is based on solving the Maxwell's equations in each layer and matching the solutions at the boundaries of the layers. To apply MF to our problem, we follow Refs. [4,49].

For monochromatic waves of frequency $\omega_0$, the Maxwell's equations can be written in the matrix form as

$$\hat{G}\mathbf{\Phi} = i\omega_0 \hat{M}\mathbf{\Phi}, \tag{A1}$$

for the generalized vector $\mathbf{\Phi} = [E_x(\boldsymbol{r}), E_y(\boldsymbol{r}), E_z(\boldsymbol{r}), H_x(\boldsymbol{r}), H_y(\boldsymbol{r}), H_z(\boldsymbol{r})]^{\mathrm{T}}$ combining the electric $E_l(\boldsymbol{r})$ and magnetic $H_l(\boldsymbol{r})$ field components, where $\boldsymbol{r} = (x, y, z)$ and $l = x, y, z$. In (A1), $\hat{G}$ is the 6×6 matrix given as

$$\hat{G} = \begin{pmatrix} \hat{0} & \hat{g} \\ -\hat{g} & \hat{0} \end{pmatrix} \quad \text{with} \quad \hat{g} = \begin{pmatrix} 0 & -\partial_z & \partial_y \\ \partial_z & 0 & -\partial_x \\ -\partial_y & \partial_x & 0 \end{pmatrix}, \tag{A2}$$

and $\hat{0}$ being the 3×3 zero matrix.

The material contribution is accounted with use of the matrix $\hat{M}$, which in the general case takes the form

$$\hat{M} = \begin{pmatrix} \hat{\varepsilon} & \hat{\rho}_1 \\ \hat{\rho}_2 & \hat{\mu} \end{pmatrix}, \tag{A3}$$

where $\hat{\varepsilon}$ and $\hat{\mu}$ are the dielectric permittivity and permeability tensors, the tensors $\hat{\rho}_{1,2}$ are responsible for optical rotation [4]. For nonmagnetic non-optically active media, $\hat{\mu} = \mu_0\hat{1}$, and $\hat{\rho}_{1,2} = \hat{0}$, where $\hat{1}$ is the identity matrix and $\mu_0$ is the vacuum permeability.

Assuming a plane wave solution of Eq. (A1), i.e., taking $\Xi(\boldsymbol{r}) = \exp[-i(\omega_0/c)(q_x x + q_y y)]\Xi(z)$, where $\Xi = E_l, H_l$ with $l = x, y, z$, and $q_{x,y}$ are the dimensionless in-plane wave vector components, we can reduce (A1) to the following form:

$$\partial_z \mathbf{\Psi}(z) = i(\omega_0/c)\hat{\Delta}\mathbf{\Psi}(z) \tag{A4}$$

for the vector $\mathbf{\Psi}(z) = [E_x(z), H_y(z), E_y(z), H_x(z)]^{\mathrm{T}}$, where the 4×4 characteristic matrix [49]

$$\hat{\Delta} = \frac{1}{\varepsilon_{zz}} \begin{pmatrix} q_x\varepsilon_{zx} & q_x^2 - \varepsilon_{zz} & q_x\varepsilon_{zy} & -q_xq_y \\ \varepsilon_{xz}\varepsilon_{zx} - \varepsilon_{xx}\varepsilon_{zz} & q_x\varepsilon_{xz} & \varepsilon_{xz}\varepsilon_{zy} - \varepsilon_{xy}\varepsilon_{zz} & -q_y\varepsilon_{xz} \\ 0 & 0 & 0 & 1 \\ \varepsilon_{yx}\varepsilon_{zz} - \varepsilon_{yz}\varepsilon_{zx} + q_xq_y\varepsilon_{zz} & -q_x\varepsilon_{yz} & \varepsilon_{yy}\varepsilon_{zz} - \varepsilon_{yz}\varepsilon_{zy} - q_x^2\varepsilon_{zz} & -q_y\varepsilon_{yz} \end{pmatrix} \tag{A5}$$

is obtained after eliminating the longitudinal components $E_z(\boldsymbol{r})$ and $H_z(\boldsymbol{r})$. The characteristic matrix does not contain the dependence of the longitudinal coordinate $z$. Thus presenting the vector $\mathbf{\Psi}(z)$ in a layer $j$ as

$$\mathbf{\Psi}_j(z) = \exp[\, i\omega_0\kappa_j z/c]\mathbf{\Psi}_j, \tag{A6}$$

where $\mathbf{\Psi}_j$ characterizes the electromagnetic field at the entrance to the layer $j$, we arrive at the eigenproblem (3) in the main text with the longitudinal (dimensionless) wave vector components $\kappa_{jm}$ as the eigenvalues and the eigenvector of the transverse field components $\mathbf{\Psi}_{jm}$, where $m = 1, 2, 3, 4$ indicates the number of the solution with four solutions in total.

Among the four eigenvalues $\kappa_{jm}$, two correspond to forward propagating waves ($\kappa_{j1}$ and $\kappa_{j2}$) in a layer $j$ while the other two correspond to backward propagating waves ($\kappa_{j3}$ and $\kappa_{j4}$). Herewith each pair contains components responsible for different wave polarizations: *s*- and *p*-polarized

waves in the absence of the external magnetic field, and ordinary and extraordinary waves in the presence of the magnetic field. See Ref. [4] for the appropriate sorting of the eigenvalues.

For operating in the basis of forward and backward propagating waves (4), the interaction matrix $\hat{A}$ should be used, which projects the electric field vector $\mathbf{E}_j$ in a layer $j$ onto the eigenmodes of the layer [4,49]. $\hat{A}$ represents a 4×4 matrix, which columns are eigenvectors of the characteristic matrix $\hat{\Delta}$. For linking the input and output boundaries of the layer, one should use the 4×4 propagation matrix, which elements are found as $P_{j,mm'} = \delta_{mm'} \exp[i(\omega_0/c)\kappa_{jm} d_j]$, where $\delta_{mm'}$ is the Kronecker delta, and $d_j$ is the thickness of the $j$th layer.


[1] K. Y. Bliokh, F. J. Rodríguez-Fortuño, F. Nori, and A. V. Zayats, Spin–orbit interactions of light, Nat. Photon. **9**, 796 (2015).

[2] I. A. Shelykh, A. V. Kavokin, Y. G. Rubo, T. C. H. Liew, and G. Malpuech, Polariton polarization-sensitive phenomena in planar semiconductor microcavities, Semicond. Sci. Technol. **25**, 013001 (2010).

[3] M. M. Glazov and L. E. Golub, Spin and transport effects in quantum microcavities with polarization splitting, Phys. Rev. B **82**, 085315 (2010).

[4] N. C. Passler and A. Paarmann, Generalized 4×4 matrix formalism for light propagation in anisotropic stratified media: Study of surface phonon polaritons in polar dielectric heterostructures, J. Opt. Soc. Am. B **34**, 2128 (2017).

[5] E. Sedov, M. Glazov, and A. Kavokin, Spin-selective currents of Tamm polaritons, Phys. Rev. Appl. **17**, 024037 (2022).

[6] A. Kavokin, J. Baumberg, G. Malpuech, and F. Laussy, *Microcavities*, 2nd ed., Series on Semiconductor Science and Technology (Oxford University Press, Oxford, 2017).

[7] D. Caputo, E. S. Sedov, D. Ballarini, M. M. Glazov, A. V. Kavokin, and D. Sanvitto, Magnetic control of polariton spin transport, Commun. Phys. **2**, 165 (2019).

[8] D. Schmidt, B. Berger, M. Kahlert, M. Bayer, C. Schneider, S. Höfling, E. S. Sedov, A. V. Kavokin, and M. Aßmann, Tracking dark excitons with exciton polaritons in semiconductor microcavities, Phys. Rev. Lett. **122**, 047403 (2019).

[9] N. Lundt, M. Klaas, E. Sedov, M. Waldherr, H. Knopf, M. Blei, S. Tongay, S. Klembt, T. Taniguchi, K. Watanabe, U. Schulz, A. Kavokin, S. Höfling, F. Eilenberger, and C. Schneider, Magnetic-field-induced splitting and polarization of monolayer-based valley exciton polaritons, Phys. Rev. B **100**, 121303(R) (2019).

[10] C. Rupprecht, E. Sedov, M. Klaas, H. Knopf, M. Blei, N. Lundt, S. Tongay, T. Taniguchi, K. Watanabe, U. Schulz *et al.*, Manipulation of room-temperature valley-coherent exciton-polaritons in atomically thin crystals by real and artificial magnetic fields, 2D Mater. **7**, 035025 (2020).

[11] K. Peng, R. Tao, L. Haeberlé, Q. Li, D. Jin, G. R. Fleming, S. Kéna-Cohen, X. Zhang, and W. Bao, Room-temperature polariton quantum fluids in halide perovskites, Nat. Commun. **13**, 7388 (2022).

[12] A. Askitopoulos, L. Mouchliadis, I. Iorsh, G. Christmann, J. J. Baumberg, M. A. Kaliteevski, Z. Hatzopoulos, and P. G. Savvidis, Bragg polaritons: Strong coupling and amplification in an unfolded microcavity, Phys. Rev. Lett. **106**, 076401 (2011).

[13] E. S. Sedov, I. V. Iorsh, S. M. Arakelian, A. P. Alodjants, and A. Kavokin, Hyperbolic metamaterials with Bragg polaritons, Phys. Rev. Lett. **114**, 237402 (2015).

[14] E. S. Sedov, E. D. Cherotchenko, S. M. Arakelian, and A. V. Kavokin, Light propagation in tunable exciton-polariton one-dimensional photonic crystals, Phys. Rev. B **94**, 125309 (2016).

[15] T. Liew, I. Shelykh, and G. Malpuech, Polaritonic devices, Phys. E **43**, 1543 (2011).

[16] E. S. Sedov, Y. G. Rubo, and A. V. Kavokin, Polariton polarization rectifier, Light Sci. Appl. **8**, 79 (2019).

[17] I. A. Shelykh, G. Pavlovic, D. D. Solnyshkov, and G. Malpuech, Proposal for a mesoscopic optical Berry-phase interferometer, Phys. Rev. Lett. **102**, 046407 (2009).

[18] I. A. Shelykh, R. Johne, D. D. Solnyshkov, and G. Malpuech, Optically and electrically controlled polariton spin transistor, Phys. Rev. B **82**, 153303 (2010).

[19] A. Kavokin, G. Malpuech, and M. Glazov, Optical spin Hall effect, Phys. Rev. Lett. **95**, 136601 (2005).

[20] C. Leyder, M. Romanelli, J. P. Karr, E. Giacobino, T. C. H. Liew, M. M. Glazov, A. V. Kavokin, G. Malpuech, and A. Bramati, Observation of the optical spin Hall effect, Nat. Phys. **3**, 628 (2007).

[21] E. S. Sedov, Y. G. Rubo, and A. V. Kavokin, *Zitterbewegung* of exciton-polaritons, Phys. Rev. B **97**, 245312 (2018).

[22] E. S. Sedov, I. E. Sedova, S. M. Arakelian, and A. V. Kavokin, Magnetic control over the *zitterbewegung* of exciton-polaritons, New J. Phys. **22**, 083059 (2020).

[23] E. Sedov, I. Sedova, S. Arakelian, and A. Kavokin, Polygonal patterns of confined light, Opt. Lett. **46**, 1836 (2021).

[24] M. Sich, L. E. Tapia-Rodriguez, H. Sigurdsson, P. M. Walker, E. Clarke, I. A. Shelykh, B. Royall, E. S. Sedov, A. V. Kavokin, D. V. Skryabin *et al.*, Spin domains in one-dimensional conservative polariton solitons, ACS Photon. **5**, 5095 (2018).

[25] M. Suffczynski, L. Swierkowski, and W. Wardzynski, Exchange splitting of direct excitons, J. Phys. C **8**, L52 (1975).

[26] G. Czajkowski and A. Tredicucci, Heavy- and light-hole excitons in anisotropic semiconductors, Il Nuovo Cimento D **14**, 1283 (1992).

[27] A. Kudelski, A. Golnik, J. A. Gaj, F. V. Kyrychenko, G. Karczewski, T. Wojtowicz, Y. G. Semenov, O. Krebs, and P. Voisin, Interface profiles and in-plane anisotropy in common anion type-I$Cd_{1-x}Mg_xTe$/CdTe/$Cd_{1-x}Mn_xTe$ heterostructures studied by reflectivity, Phys. Rev. B **64**, 045312 (2001).

[28] A. A. Toropov, E. L. Ivchenko, O. Krebs, S. Cortez, P. Voisin, and J. L. Gentner, Excitonic contributions to the quantum-confined Pockels effect, Phys. Rev. B **63**, 035302 (2000).

[29] E. L. Ivchenko, A. Y. Kaminski, and U. Rössler, Heavy-light hole mixing at zinc-blende (001) interfaces under normal incidence, Phys. Rev. B **54**, 5852 (1996).

[30] R. Balili, B. Nelsen, D. W. Snoke, R. H. Reid, L. Pfeiffer, and K. West, Huge splitting of polariton states in microcavities under stress, Phys. Rev. B **81**, 125311 (2010).

[31] A. V. Larionov, V. D. Kulakovskii, S. Höfling, C. Schneider, L. Worschech, and A. Forchel, Polarized nonequilibrium bose-einstein condensates of spinor exciton polaritons in a magnetic field, Phys. Rev. Lett. **105**, 256401 (2010).

[32] E. S. Sedov and A. V. Kavokin, Artificial gravity effect on spin-polarized exciton-polaritons, Sci. Rep. **7**, 9797 (2017).

[33] S. Morina, T. C. H. Liew, and I. A. Shelykh, Magnetic field control of the optical spin Hall effect, Phys. Rev. B **88**, 035311 (2013).

[34] R. Johne, I. A. Shelykh, D. D. Solnyshkov, and G. Malpuech, Polaritonic analogue of Datta and Das spin transistor, Phys. Rev. B **81**, 125327 (2010).

[35] D. Loginov, V. Kochereshko, R. Cox, L. Besombes, H. Mariette, J. Davies, D. Wolverson, and L. Smith, Excitonic polaritons in transverse magnetic fields, Phys. Status Solidi B **247**, 1528 (2010).

[36] K. Rechcińska, M. Król, R. Mazur, P. Morawiak, R. Mirek, K. Łempicka, W. Bardyszewski, M. Matuszewski, P. Kula, W. Piecek, P. G. Lagoudakis, B. Pietka, and J. Szczytko, Engineering spin-orbit synthetic Hamiltonians in liquid-crystal optical cavities, Science **366**, 727 (2019).

[37] M. Król, K. Rechcińska, H. Sigurdsson, P. Oliwa, R. Mazur, P. Morawiak, W. Piecek, P. Kula, P. G. Lagoudakis, M. Matuszewski *et al.*, Realizing optical persistent spin helix and Stern-Gerlach deflection in an anisotropic liquid crystal microcavity, Phys. Rev. Lett. **127**, 190401 (2021).

[38] T. Long, X. Ma, J. Ren, F. Li, Q. Liao, S. Schumacher, G. Malpuech, D. Solnyshkov, and H. Fu, Helical polariton lasing from topological valleys in an organic crystalline microcavity, Adv. Sci. **9**, 2203588 (2022).

[39] K. Łempicka-Mirek, M. Król, H. Sigurdsson, A. Wincukiewicz, P. Morawiak, R. Mazur, M. Muszyński, W. Piecek, P. Kula, T. Stefaniuk *et al.*, Electrically tunable Berry curvature and strong light-matter coupling in liquid crystal microcavities with 2D perovskite, Sci. Adv. **8**, eabq7533 (2022).

[40] K. Łempicka Mirek, M. Król, L. D. Marco, A. Coriolano, L. Polimeno, I. Viola, M. Kedziora, M. Muszyński, P. Morawiak, R. Mazur *et al.*, Electrical polarization switching of perovskite polariton laser, Nanophotonics (2024).

[41] M. Muszyński, M. Król, K. Rechcińska, P. Oliwa, M. Kdziora, K. Łempicka-Mirek, R. Mazur, P. Morawiak, W. Piecek, P. Kula, P. G. Lagoudakis, B. Pietka, and J. Szczytko, Realizing persistent-spin-helix lasing in the regime of Rashba-Dresselhaus spin-orbit coupling in a dye-filled liquid-crystal optical microcavity, Phys. Rev. Appl. **17**, 014041 (2022).

[42] R. Su, A. Fieramosca, Q. Zhang, H. Nguyen, E. Deleporte, Z. Chen, D. Sanvitto, T. Liew, and Q. Xiong, Perovskite semiconductors for room-temperature exciton-polaritonics, Nat. Mater. **20**, 1315 (2021).

[43] E. Sedov, I. Sedova, S. Arakelian, G. Eramo, and A. Kavokin, Hybrid optical fiber for light-induced superconductivity, Sci. Rep. **10**, 8131 (2020).

[44] A. Fieramosca, L. Polimeno, V. Ardizzone, L. Marco, M. Pugliese, V. Maiorano, M. D. Giorgi, L. Dominici, G. Gigli, D. Gerace, D. Ballarini, and D. Sanvitto, Two-dimensional hybrid perovskites sustaining strong polariton interactions at room temperature, Sci. Adv. **5**, eaav9967 (2019).

[45] The parameters of the materials of the structure are taken as following. The refractive indices of the DBRs are $n_{SiO_2} = 1.456$ and $n_{TiO_2} = 2.436$. The LC dielectric constants are $\varepsilon_{\parallel} = 1.539^2$ and $\varepsilon_{\perp} = 1.949^2$.

[46] P. Yeh, Electromagnetic propagation in birefringent layered media, J. Opt. Soc. Am. **69**, 742 (1979).

[47] D. W. Berreman, Optics in stratified and anisotropic media: 4×4-matrix formulation, J. Opt. Soc. Am. **62**, 502 (1972).

[48] W. Xu, L. T. Wood, and T. D. Golding, Optical degeneracies in anisotropic layered media: Treatment of singularities in a 4×4 matrix formalism, Phys. Rev. B **61**, 1740 (2000).

[49] G. D. Landry and T. A. Maldonado, Gaussian beam transmission and reflection from a general anisotropic multilayer structure, Appl. Opt. **35**, 5870 (1996).

[50] N. C. Passler, M. Jeannin, and A. Paarmann, Layer-resolved absorption of light in arbitrarily anisotropic heterostructures, Phys. Rev. B **101**, 165425 (2020).

[51] G. Dresselhaus, Spin-orbit coupling effects in zinc blende structures, Phys. Rev. **100**, 580 (1955).

[52] E. I. Rashba and V. I. Sheka, Symmetry of energy bands in crystals of wurtzite type. II. Symmetry of bands with spin-orbit interaction included, Fiz. Tverd. Tela: Collected Papers **2**, 162 (1959).

[53] M. Dyakonov and V. Kachorovskii, Spin relaxation of two-dimensional electrons in noncentrosymmetric semiconductors, Soviet Phys. Semiconductors **20**, 110 (1986).

[54] S. D. Ganichev and L. E. Golub, Interplay of Rashba/Dresselhaus spin splittings probed by photogalvanic spectroscopy—A review, Phys. Status Solidi B **251**, 1801 (2014).

[55] M. I. Dyakonov, *Spin Physics in Semiconductors*, 2nd ed., Springer Series in Solid-State Sciences 157 (Springer International Publishing, New York, 2017).

[56] L. Karpa and M. Weitz, A Stern–Gerlach experiment for slow light, Nat. Phys. **2**, 332 (2006).

[57] G. Panzarini, L. C. Andreani, A. Armitage, D. Baxter, M. S. Skolnick, V. N. Astratov, J. S. Roberts, A. V. Kavokin, M. R. Vladimirova, and M. A. Kaliteevski, Exciton-light coupling in single and coupled semiconductor microcavities: Polariton dispersion and polarization splitting, Phys. Rev. B **59**, 5082 (1999).

[58] S. A. Tarasenko, A. V. Poshakinskiy, E. L. Ivchenko, I. Stepanov, M. Ersfeld, M. Lepsa, and B. Beschoten, Zitterbewegung of spin split electrons, JETP Lett. **108**, 326 (2018).